Comparing synthetic refocusing to deconvolution for the extraction of neuronal calcium transients from light fields

Carmel L. Howe◉,[a,b] Peter Quicke◉,[a,b] Pingfan Song,[b,c]
Herman Verinaz-Jadan◉,[b,c] Pier Luigi Dragotti◉,[b,c] and
Amanda J. Foust◉[a,b,*]

[a]Imperial College London, Department of Bioengineering, London, United Kingdom
[b]Imperial College London, Centre for Neurotechnology, London, United Kingdom
[c]Imperial College London, Department of Electrical and Electronic Engineering, London, United Kingdom

Abstract

Significance: Light-field microscopy (LFM) enables fast, light-efficient, volumetric imaging of neuronal activity with calcium indicators. Calcium transients differ in temporal signal-to-noise ratio (tSNR) and spatial confinement when extracted from volumes reconstructed by different algorithms.

Aim: We evaluated the capabilities and limitations of two light-field reconstruction algorithms for calcium fluorescence imaging.

Approach: We acquired light-field image series from neurons either bulk-labeled or filled intra-cellularly with the red-emitting calcium dye CaSiR-1 in acute mouse brain slices. We compared the tSNR and spatial confinement of calcium signals extracted from volumes reconstructed with synthetic refocusing and Richardson–Lucy three-dimensional deconvolution with and without total variation regularization.

Results: Both synthetic refocusing and Richardson–Lucy deconvolution resolved calcium signals from single cells and neuronal dendrites in three dimensions. Increasing deconvolution iteration number improved spatial confinement but reduced tSNR compared with synthetic refocusing. Volumetric light-field imaging did not decrease calcium signal tSNR compared with interleaved, widefield image series acquired in matched planes.

Conclusions: LFM enables high-volume rate, volumetric imaging of calcium transients in single cell somata (bulk-labeled) and dendrites (intracellularly loaded). The trade-offs identified for tSNR, spatial confinement, and computational cost indicate which of synthetic refocusing or deconvolution can better realize the scientific requirements of future LFM calcium imaging applications.

1 Introduction

Understanding how neuronal networks learn, process, and store information requires imaging techniques capable of monitoring the activity of hundreds to thousands of neurons simultaneously in three-dimensional (3D) tissues. Capturing rapid neuronal calcium dynamics requires high temporal resolution at cellular or subcellular spatial resolution.[1] The development of

---

*Address all correspondence to Amanda J. Foust, a.foust@imperial.ac.uk

synthetic and genetically encoded fluorescent indicators of intracellular calcium concentration[2,3] and membrane voltage[4,5] enables functional imaging on these scales.

The optical sectioning capability of confocal and multiphoton scanning microscopes adapts them well to 3D imaging of scattering brain tissues. However, scanning limits the fluorescence bandwidth and hence the acquisition speed and temporal signal-to-noise ratio (tSNR). tSNR describes the ability to discriminate transient changes in fluorescence from baseline noise. For shot noise-limited systems, tSNR is proportional to the square-root of the collected fluorescence photon flux. That is why applications requiring high acquisition rates and/or SNR typically rely on widefield, single-photon imaging to maximize photon flux by exciting fluorescence simultaneously in all illuminated structures. Widefield excites fluorescence efficiently throughout a volume, however, only one axial plane is in focus. In this configuration, fluorescence excited above and below the imaging plane is not only unnecessary but also contributes spurious fluorescence to the in-focus image, degrading contrast and confusing the functional signals.[6]

Light-field microscopy (LFM) exploits out-of-focus fluorescence simultaneously excited throughout the volume. LFM combined with widefield, single-photon fluorescence excitation enables volumetric collection, maximizing the photon budget. LFM is a 3D imaging technique, which encodes both lateral position and angular information, unlike conventional imaging that focuses on objects in a single plane.[7] A microlens array (MLA) at the microscope's native image plane enables image reconstruction at different planes and perspectives from a single light-field image. This increases light efficiency and speed at the cost of spatial resolution as the camera's pixels now divide over four-dimensions $(x, y, \theta_x, \theta_y)$ rather than two (x, y). The four-dimensional (4D) light-field can be used to reconstruct a volume around the native focal plane, slice by slice. Two methods for reconstructing volumes from LFM images are commonly used: synthetic refocusing[7] and 3D deconvolution.[8] Synthetic refocusing extracts single planes from a light-field that correspond to widefield images. Multiple planes can be reconstructed orthogonal to the optical axis to generate a z-stack. Synthetic refocusing is computationally fast as each pixel in the output volume is simply the weighted sum of a subset of pixels in the light-field. However, similar to widefield imaging, this technique lacks optical sectioning such that out-of-focus sources reduce the contrast of in-focus sources. In contrast, 3D deconvolution reconstructs a volume by deconvolving its light-field measurements with a 3D light-field point spread function (PSF) based on a wave optics model[9] of the LFM. This can be achieved using iterative deconvolution methods, such as the Richardson–Lucy (RL)[10,11] or image space reconstruction algorithms.[12] 3D deconvolution can achieve a higher spatial resolution than synthetic refocusing because the individual projections through the volume sample the object more finely than the MLA, thus improving the discrimibility of signals in 3D. However, 3D deconvolution approaches are computationally intensive and amplify noise.[13]

LFM's capacity to capture volumetric data from 2D frames has recently motivated its application to imaging neuronal activity in nonscattering specimens such as *C. elegans* and Zebrafish,[14–19] and in mammalian brain *in vivo*.[20–22] Seeded iterative demixing[20,22] and compressive LFM[15] increase the speed of neuronal localization and single-cell time series analysis by identifying and localizing somatic signals. Notably, these techniques improved performance in scattering brain tissues compared to volume reconstruction methods that only account for ballistic photons. However, volume reconstruction is still necessary to image the generation and propagation of voltage and calcium transients in spatially extended structures such as axons and dendrites.

Here we show that LFM can resolve calcium transients simultaneously in axially separated somata and dendrites of neurons loaded with a red-emitting calcium dye, CaSiR-1.[23] We examined trade-offs between the tSNR and the spatial signal confinement of calcium signals localized in volumes reconstructed from light fields by synthetic refocusing and 3D deconvolution. A comparison of calcium signals extracted from interleaved light-field and widefield imaging trials showed no penalty to tSNR for light-field trials, which additionally enabled localization of calcium signals in 3D. These results demonstrate the power of LFM for simultaneously tracking calcium transients in axially separated neurons and neuronal subcompartments. By distilling the trade-offs between spatial signal confinement and tSNR, these results underline the importance of selecting a volume reconstruction method adapted to the scientific goals of future experiments.

2 Materials and Methods

Parts of the following methods and preliminary tSNR quantification results were published in Ref. 24.

2.1 Optical System

We designed our LFM following Levoy et al.[7] Imaging was performed with a custom-built epifluorescence microscope with an MLA (125 μm pitch, f/10, RPC Photonics) placed at the imaging plane of a 25×, numerical aperture (NA) = 1.0 water immersion objective lens (XLPLN25XSVMP, Olympus), and 180-mm tube lens (TTL180-A, Thorlabs), shown in Fig. 1(a). The MLA was imaged onto a scientific complementary metal–oxide–semiconductor (sCMOS) camera (ORCA Flash 4 V2 with Camera Link, 2048 × 2048 pixels, 6.5 μm pixel size, Hamamatsu) with a 1:1 relay macro lens (Nikon 60 mm f2.8 D AF Micro Nikkor Lens). The MLA was aligned following the advice in Zhang (2010) with a 660-nm light-emitting diode (LED) (M660L2, Thorlabs).[25]
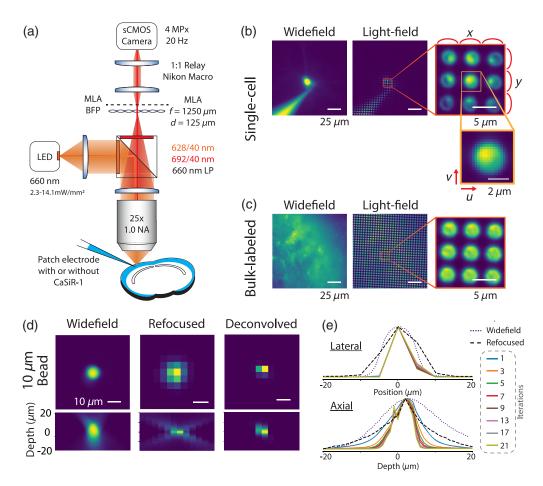

Fig. 1 (a) Optical system schematic. An MLA is placed at the native imaging plane of a widefield microscope and the back focal plane is imaged onto an sCMOS camera enabling 3D reconstructions from a 2D frame. (b) Example widefield and light-field images from both a single neuron intracellularly loaded with the synthetic calcium dye, CaSiR-1 via a micropipette. Close-up views of the raw light-field images show the circular subimages encoding the 4D spatial and angular information. The light-field is parameterized by a 4D function, $\mathcal{L}(u, v, x, y)$, where each lenslet is $\mathcal{L}(u, v, \cdot, \cdot)$ and the same pixel in each lenslet subimage is $\mathcal{L}(\cdot, \cdot, x, y)$. (c) Example images from bulk-labeled slices where CaSiR-1 AM was bath applied to many neurons. (d) Example widefield and reconstructed light-field images from a 10 μm fluorescent bead fixed in agarose. (e) The lateral and axial profiles of the bead with widefield (dotted line), synthetic refocusing (dashed line), and RL deconvolution up to 21 iterations (solid lines, iteration number indicated by color code).

The LFM image consists of circular subimages [Fig. 1(b)] which are parameterized by the 4D function $\mathcal{L}(u, v, x, y)$, where each lenslet is $\mathcal{L}(u, v, \cdot, \cdot)$ and the same pixel in each lenslet subimage is $\mathcal{L}(\cdot, \cdot, x, y)$. Each circular subimage represents the angular content of the light at a specific spatial location.

The "native LFM spatial resolution" is given by the microlens pitch divided by the objective magnification. Therefore, an MLA was chosen such that the lateral resolution of our LFM was 5 μm, roughly half the diameter of a cortical neuron (10 μm). The axial resolution of a LFM is defined by the number of resolvable diffraction-limited spots behind each microlens.[7] Using the Sparrow criterion and assuming a peak emission wavelength of 664 nm (λ) for CaSiR-1,[23] the spot size in the camera plane is 7.8 μm. So, with a 125 μm pitch MLA, we are able to resolve $N_u = 16$ distinct spots under each microlens. The depth-of-field when synthetically refocusing is given by Eq. (1), resulting in a depth-of-field of 7.96 μm[7] compared to 0.9 μm in a conventional widefield microscope with the same imaging parameters:

$$D = \frac{(2 + N_u)\lambda n}{2NA^2},$$ (1)

where n is the refractive index.

2.2 Brain Slice Preparation

This study was carried out in accordance with the recommendations of the UK Animals (Scientific Procedures) Act 1986 under Home Office Project and Personal Licenses (project license 70/9095). 400 μm slices were prepared from 33- to 196-day old mice using the "protective recovery" method.[26] Slices were cut in Na-aCSF containing (in mM): 125 NaCl, 25 NaHCO$_3$, 20 glucose, 2.5 KCl, 1.25 NaH$_2$PO$_4$, 2 MgCl$_2$, 2 CaCl$_2$. After cutting, the slices were transferred for a period of 12 min to a solution containing (in mM) 110 N-methyl-d glucamine, 2.5 KCl, 1.2 NaH$_2$PO$_4$, 25 NaHCO$_3$, 25 glucose, 10 MgCl$_2$, 0.5 CaCl$_2$, adjusted to 300 to 310 mOsm/kg, pH 7.3 to 7.4 with HCl at 36°C, before being transferred back to the first solution for at least an hour before imaging trials. All solutions were oxygenated with 95%O$_2$/5%CO$_2$.

After resting the slices were either bulk-labeled with CaSiR-1 AM-ester dye or used for single-cell labeling with CaSiR-1 potassium salt.

For bulk-labeled slices 50 μg, CaSiR-1 AM (GC402, Goryo Chemicals)[23] was dissolved in 10 μL of dimethyl sulfoxide (DMSO) with 10% w/v Pluronic F-127 (Invitrogen) and 0.5% v/v Kolliphor EL (Sigma-Aldrich).[27] The slices were then incubated for 40 min at 37°C in 2 mL of Na-aCSF with the CaSiR-1 AM/DMSO mixture pipetted onto the surface of each slice, oxygenated by blowing 95%O$_2$/5%CO$_2$ onto the surface. After loading, the slices rested in room temperature Na-aCSF for at least 20 min before use.

2.3 Imaging

For single-cell labeling, cortical cells were patched using 6 to 8 MOhm patch pipettes containing intracellular solution consisting of (in mM): 130 K-Gluconate, 7 KCl, 4 ATP-Mg, 0.3 GTP-Na, 10 Phosphocreatine-Na, 10 HEPES, 0.1 CaSiR-1 potassium salt (GC401, Goryo Chemicals).[23] After sealing and breaking in, the calcium dye was allowed to diffuse into the cell [Fig. 1(b)]. For bulk-labeled slices [Fig. 1(c)], cortical cells were patched containing the same intracelluar solution without the addition of the CaSiR-1 potassium salt.

Cells were patched under oblique LED infrared illumination (peak 850 nm). The signals were recorded with a Multiclamp 700B amplifier (Axon Instruments) and digitized with a Power 1401 (Cambridge Electronic Design).

Imaging trials were taken at 20 frames/s at room temperature. Stimulation consisted of five current pulses for 10 ms at 0.5 Hz where the current was adjusted to stimulate a single action potential. For single cells, this stimulus was applied to the labeled cell with the dye-loading pipette. For bulk-labeled slices, the stimulus was applied to a cell in the field of view causing broader activation of multiple neurons in the local network. Widefield and light-field trials were interleaved by removing and replacing the MLA from a precision magnetic mount

(CP44F, Thorlabs). The removal and addition of the MLA shifted the focal sample plane. We calculated this focal plane shift using the thin lens equation to be ± 2 μm.

Fluorescence was excited with a 660-nm LED (M660L2, Thorlabs) powered by a constant current source (Keithley Sourcemeter 1401) to illuminate the sample between 2.3 and 14.1 mW/mm^2. The 660-nm LED was collimated with an $f = 16$ mm aspheric lens (ACL25416U0-A, Thorlabs) and filtered with a 628/40-nm excitation filter (FF02-628/40, Semrock). Collected fluorescence was filtered with a 660-nm long-pass dichroic (FF660-Di02, Semrock) along with a 692/40-nm emission filter (FF01-692/40, Semrock). Imaging data were acquired with Micromanager.[28]

Single-cell labeled somata laid between 46 and 49 μm below the slice surface, with a median depth of 47 [IQR, 46.2, 48.6] μm. Whereas bulk-labeled somata were between 29 and 36 μm below the slice surface, with a median depth of 34 [30, 34.8] μm.

2.4 Light-Field Volume Reconstruction

We reconstructed light-field source volumes from the raw light-fields [Figs. 1(b) and 1(c)] using synthetic refocusing[7] and RL 3D deconvolution.[8,10,11] Images synthetically refocused at a plane $f' = \alpha f_0$, where f_0 is the native focal plane, were calculated from a light-field image parameterized by $\mathcal{L}(x, y, u, v)$ using the formula derived in Ref. 29 as

$$I(x, y) = \sum_{u,v} \mathcal{L}(x + u(1 - 1/\alpha), y + v(1 - 1/\alpha), u, v), \tag{2}$$

where $I(x, y)$ represents the refocused image. This process can be interpreted as a summation over different shifted angular "views" of the sample represented by $\mathcal{L}(x, y, \cdot, \cdot)$ such that the rays forming the views intersect at the desired refocus plane. We synthetically refocused "stacks" of images or image time series, $I(x, y, z, t)$ at 1 μm z-intervals using linear interpolation of the collected light-field images or videos.

Stacks from the same light-field images were also calculated using RL deconvolution. The 3D light-field PSF was calculated using the method described in Ref. 9, by considering how an LFM collects fluorescence from a dipole oscillating with a wavelength of 660 nm. The total PSF was calculated as an incoherent sum of dipoles oriented along x, y, and z. PSF values were calculated on a 5×5 grid relative to the microlens. A low resolution PSF was calculated by averaging over the PSF values weighted by a 2D Hamming window of a width equal to the MLA pitch and coaxial with the lens. The estimated volume, x, is recovered from the measured light-field image, y, and the PSF, H using the following iterative update scheme in matrix-vector notation:

$$x^{k+1} = \frac{1}{a} \left[H^T \frac{y}{Hx^k} \right] x^k, \tag{3}$$

where the fraction y/Hx^k is computed elementwise and $a = \sum_i H(i, :)$. Stacks were reconstructed using this method as with synthetic refocusing for varying numbers of iterations of Eq. (3).

In addition, to enhance edges and reduce noise, we slightly modified the objective function of RL to include a total variation (TV) term.[30] Including a total variation term in the objective function imposes a sparsity constraint on the image gradient. Therefore, an image with low total variation has large regions with close-to-zero gradients (denoised regions) and some with non-zero gradients (edges). To incorporate this regularization prior, we modified the standard RL as follows:

$$x^{k+1} = H^T \left(\frac{y}{Hx} \cdot \frac{x^k}{a - \lambda \text{div}\left(\frac{\nabla x^k}{|\nabla x^k|}\right)} \right), \tag{4}$$

where div is the divergence operator, ∇ is the gradient operator, and λ is a regularization factor set to 0.01, determined by visual inspection of the volumes.

2.5 Time Series Analysis

2.5.1 tSNR

Signals were extracted from widefield or light-field time series reconstructed with synthetic refocusing or RL 3D deconvolution, at the plane of best focus unless otherwise specified.

We calculated $\Delta F/F$ using Eq. (5) where F was the raw fluorescent signal, F_0 was the baseline fluorescence taken as an average prior to the action potential, and F_d was the camera's dark signal (all in counts):

$$\frac{\Delta F}{F} = \frac{F - F_0}{F_0 - F_d}. \tag{5}$$

An "activation map" was produced from the variance over time to indicate the pixels containing the greatest temporal signal from the $\Delta F/F$ map. Regions of interest (ROIs) were defined by extracting the top 2 percentile of signal containing pixels (somatic and dendritic).

In the figures, contours were plotted around the ROIs as follows. First, a binary mask was created with the coordinates of the signal-containing pixels as determined with the 2% threshold condition. Next, a binary dilation operation was performed on this binary mask. The result from the binary dilation and the binary mask were combined by an XOR function to generate an expanded outline. This outline was plotted as an overlay on the activation maps.

The tSNR was calculated by dividing the peak signal (%) by the baseline noise (%), given by the square-root of the variance of the baseline fluorescence taken as an average prior to the action potential (20 samples, 1 s).

2.6 Statistics

All statistics are reported as median [interquartile range (IQR)]. Wilcoxon matched-pairs signed-rank test was performed between synthetically refocused and 3D deconvolved light-field time series. These reconstructions were generated from the same image series, removing independent variables such as bleaching and changes in dye loading in the case of single-cell labeling. Statistical analysis was performed using Python SciPy.[31]

2.7 Signal Confinement

2.7.1 Spatial profiles

To compare the signal confinement, spatial profiles were generated. To produce the widefield axial profile, a z-stack was collected manually. At the end of an imaging trial, the micropipette was removed and a z-stack was collected by moving the plane of focus through the sample between -40 and $40~\mu$m in steps of $1~\mu$m using a stepper motor. Light-field axial profiles (xz, yz) were generated by synthetically refocusing and deconvolving at different depths from the light field taken with the cell in the native imaging plane. Lateral profiles (x and y) were then generated by taking a line plot through the cell on widefield or reconstructed light-field images at the plane of best focus. The spatial signal confinement is reported from the full-width at half-maximum (FWHM). Friedman's two-way analysis of variance by ranks was performed between the FWHMs from widefield and light-field volumes reconstructed with synthetic refocusing and three-iteration RL 3D deconvolution.

The spatial profiles from single-cells were generated from either a single static image in the case of light-field frames or a stack of widefield frames. However, in bulk-labeled slices, the background signal was very large and the spatial profiles were generated from the activation map described in Sec. 3. Maximum intensity projections were taken through x, y, xz, and yz. Spatial profiles from a red fluorescence 10 μm bead (ThermoFisher, F8831, exc. 625 nm, emi. 645 nm) fixed in agarose were extracted from widefield and reconstructed light-fields [Figs. 1(d) and 1(e)].

2.7.2 *Temporal spatial profiles*

Temporal spatial profiles were produced from single cells to determine the axial spread of the calcium fluorescence response. Light-field axial profiles were generated as in Sec. 2.7.1. Time courses were extracted for each depth from either a somatic or nearby dendritic ROI. $\Delta F/F$ was calculated using Eq. (5) in Sec. 2.5.1. A line plot across the axial range was generated from the sum over time.

3 Results

3.1 *Synthetic Refocusing Enables Fast, High tSNR Light-Field Reconstruction*

We compared the performance of light-field reconstruction techniques on the tSNR of CaSIR-1 signals extracted from both single-cell (intracellularly loaded) and bulk-labeled slices. We reconstructed volumetric light-field time series from four single cells [Fig. 2(a) and Video 1) and four bulk-labeled slices [Fig. 2(b)] with synthetic refocusing and RL 3D deconvolution. For single-cell trials, calcium transients were stimulated by applying suprathreshold current pulses (red lines) to the soma in whole-cell current clamp [Fig. 2(a2)]. Calcium transients from bulk-labeled slices were captured after a single cell was stimulated within the field of view [Fig. 2(a2)]. We interleaved widefield and light-field acquisitions by swapping the MLA in and out of the light path to facilitate comparison of functional signals extracted from matched ROIs. Time courses were extracted from an ROI taken from the top 2 percentile of pixels at the native focal plane. The tSNR, peak signal, and baseline noise were compared between the two light-field reconstruction algorithms and widefield image series.

Iterative 3D deconvolution algorithms including RL are known to amplify noise,[30] which increases with iteration number. Therefore, we quantified the effect of iteration number on the peak signal, noise, and tSNR from single-cell trials. Light-field time series were deconvolved with between 1 and 21 iterations. The deconvolution was stopped at 21 iterations, before convergence, to limit noise amplification. Early stopping provides a regularizing effect on the deconvolution.[13,32] The deconvolved time series were normalized to synthetically refocused time series generated from the same raw light-fields. On average, the peak signal (%) increases with iteration number with respect to synthetically refocused light-field time series [Fig. 2(c1)]. As iteration number increases, the deconvolved peak signal increases to a peak signal around 3× greater than that achieved by synthetic refocusing at 21 iterations. In all trials, as iteration number increases, the noise (%) increases compared to synthetically refocused light-field time series [Fig. 2(c2)]. The deconvolved time series noise was on average the same as synthetically refocused light-field time series after 1 iteration increasing to 3× greater with 21 iterations. Therefore, on average, as iteration number increases the tSNR reduces [Fig. 2(c3)]. The tSNR from deconvolved light-field time series after 1 iteration is on average 1.5× larger than that of synthetically refocused light-field time series. The tSNR from deconvolved and synthetically refocused trials is the same around 17 iterations. Next, we compared the performance of light-field reconstruction techniques on the tSNR from all trials for both single-cell and bulk-labeled slices. Three-iteration RL deconvolution was chosen to give the best lateral signal confinement at the highest possible tSNR, as detailed in the next section.

The peak signal from single-cell trials (nine trials, four cells, three mice) was significantly larger when extracted from light-field time series reconstructed with three-iteration RL 3D deconvolution (16.7 [10.9, 23.5]%) compared to synthetic refocusing (11.3 [5.9, 14.7]%; Wilcoxon matched pairs signed rank, $n = 9$, $w = 36.0$, $p = 0.01$) and single-plane widefield time series (3.2 [1.7, 5.6]%; Fig. 2(d1)). The baseline noise did not differ between light-field time series reconstructed with three-iteration 3D deconvolution (0.34 [0.24, 0.44]%), those reconstructed with synthetic refocusing (0.31 [0.20, 0.55]%; Wilcoxon matched pairs signed rank, $n = 8$, $w = 15.0$, $p = 0.4$), and those from widefield time series (0.10 [0.04, 0.26]%; Fig. 2(d2)). The tSNR of times series from three-iteration RL-deconvolved frames (46.0 [35.7, 86.0]) was significantly greater than that of synthetically refocused frames (29.9 [17.8, 49.9]; Wilcoxon rank sum, $n = 8$, $w = 25.0$, $p = 0.01$) and single-plane widefield time series (21.9 [16.8, 86.2]; Fig. 2(d3)).
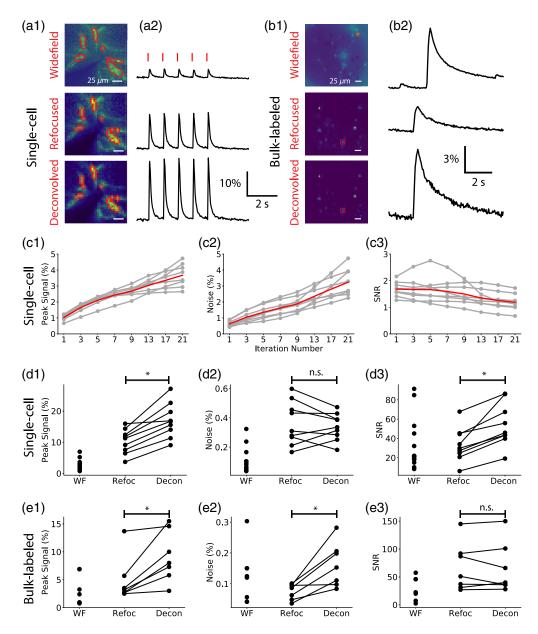
Fig. 2 A comparison of calcium transient tSNR for widefield (WF) and light fields reconstructed with synthetic refocusing or RL 3D deconvolution. (a1), (b1) The calcium activation maps of planes reconstructed from light fields containing (a1) a single labeled cell and (b1) multiple cells in bulk-labeled slices using synthetic refocusing and RL 3D deconvolution (three-iteration) algorithms. Widefield bulk-labeled images were plotted from single plane activation maps whereas light-field were from maximum intensity projections through z. (a2), (b2) Calcium transient time series were extracted from the mean pixel intensities of the ROIs (outlined in red). As deconvolution iteration number increases, so does (c1) the peak signal and (c2) noise respective to time series reconstructed with synthetic refocusing for matching ROIs, ultimately reducing (c3) the tSNR. The gray traces are from separate single-cell experiments and the red line is the average ($n = 4$ cells). (c1)–(c3) Normalized by the signal, noise, and tSNR of signals extracted from the same ROIs in the synthetically refocused planes. (d), (e) Comparison of peak signal (%), noise (%), and tSNR between time series extracted from WF images series, refocused and deconvolved (three-iteration RL) light fields (Video 1, mp4, 8628 KB [URL: https://doi.org/10.1117/1.NPh.9.4 .041404.1]).

In bulk-labeled slices (seven trials, six cells, two mice), the peak signal was significantly greater for light-field time series reconstructed with three-iteration RL 3D deconvolution (8.0 [4.7, 15.0]%) compared to synthetically refocused (3.2 [2.6, 8.9]%; Wilcoxon rank sum, $n = 7$, $w = 0.0$, $p = 0.02$) and widefield time series (1.7 [0.8, 5.1]%; Fig. 2(e1)). The baseline noise was significantly larger in three-iteration deconvolved bulk-labeled slices (0.15 [0.09, 0.24]%) compared to synthetic refocusing (0.09 [0.04, 0.10]%; Wilcoxon rank sum, $n = 7$, $w = 0.0$, $p = 0.02$), and widefield time series (0.12 [0.05, 0.22]%; Fig. 2(e2)). The tSNR from light-field time series reconstructed with synthetic refocusing (51.0 [29.5, 112.9]) did not differ from deconvolution-reconstructed trials (40.4 [32.6, 120.7]; Wilcoxon rank sum, $n = 5$, $z = 14.0$, $p = 1.0$) or widefield trials (21.1 [4.9, 51.7]), Fig. 2(e3)).

To enhance edges and reduce noise in bulk-labeled volumes, we modified the objective function of RL to include a TV regularization term (Fig. S1A in the Supplemental Material). Inclusion of the TV term in the RL deconvolution reduced the total variation of the deconvolved stacks from 0.158 to 0.128 after 10 iterations with a regularization factor of 0.01. However, the mean squared error between TV and non-TV reconstructed volumes was very small, resulting in identical peak signal, noise, and tSNR in the extracted calcium time series (Fig. S1B in the Supplemental Material). Increasing iteration number up to 30 increased peak signal, and thus tSNR, for the TV-regularized volume (Fig. S1C in the Supplemental Material).

3.2 Deconvolution Reconstruction Algorithms Provide Enhanced Spatial Signal Confinement

We compared the lateral and axial signal confinement of single cells intracellularly labeled with calcium dye between widefield z-stacks and 3D light-fields reconstructed with synthetic refocusing [Fig. 3(a2)] and RL 3D deconvolution [Fig. 3(a3) and Video 2]. To assess the impact of deconvolution iteration number on spatial confinement, we measured the FWHM of lateral and axial profiles, normalized to the FWHM the same profiles in synthetically refocused volumes. Both the lateral [Fig. 3(b1)] and axial [Fig. 3(b2)] signal confinement increase with increasing deconvolution iteration number. The red line shows the average for the three cells. The lateral signal confinement [Fig. 3(b1)] for one iteration is around 1.2× better than synthetically refocused light-field images and plateaus around 10 iterations with a 1.5× improvement. The axial signal confinement [Fig. 3(b2)] for one deconvolution iteration is 1.1× better than synthetic refocusing increasing to 2.2× after 21 deconvolution iterations. Three-iteration RL deconvolution was chosen for further analysis as it maximized lateral confinement while maintaining a high tSNR.

The 2D spatial profiles [Figs. 3(a1)–3(a3)] clearly show that the light-field images reconstructed with 3D deconvolution have better spatial signal confinement, both laterally and axially compared to both those reconstructed with synthetic refocusing and widefield stacks. The spatial profile for refocused volumes looks similar to widefield, which is expected due to the nature of the reconstruction. A line plot was taken through the lateral and axial profiles, and the FWHM was calculated for each of the imaging configurations from three cells [Figs. 3(c1) and 3(c2)]. The results are summarized in Table 1.

The lateral signal confinement [x and y; Fig. 3(c1)] from light-field images reconstructed with 3D deconvolution (three-iteration RL) was better than that of synthetically refocused or widefield stacks (Friedman's two-way analysis of variance by ranks; x: $n = 3$, $w = 2.67$, $p = 0.26$ y: $n = 3$, $w = 6.00$, $p = 0.05$). Moreover, 3D deconvolution significantly improved axial signal confinement [xz; Fig. 3(c2)] compared with that of synthetically refocused or widefield stacks (Friedman's two-way analysis of variance by Ranks; $n = 3$, $w = 6$, $p < 0.05$).

For the bulk-labeled slices, the low contrast of the raw images precluded segmentation of individual cells. The cellular spatial profiles were therefore generated from an activation map (the variance of $\Delta F/F$ over time). Maximum intensity projections through xz and yz are shown for synthetically refocused [Fig. 4(a)] and deconvolved [three iterations; Fig. 4(b)] volume reconstructions of the variance of the light-field functional time series. The signal confinement for both synthetically refocused and 3D deconvolved light-field volumes enabled resolution of a number of active neurons across different focal planes spanning about 9 μm, which is
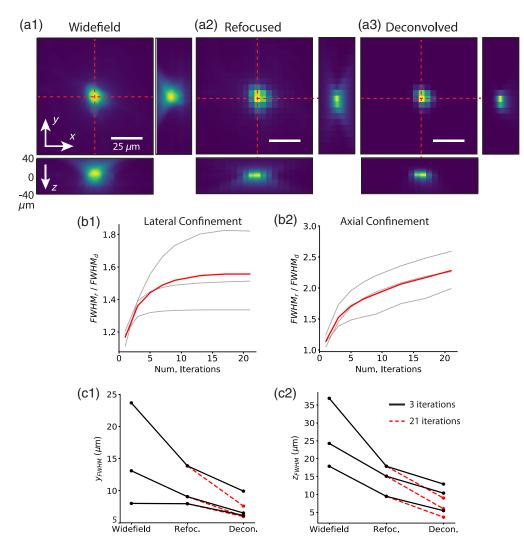
Fig. 3 Deconvolution enhances spatial signal confinement compared to widefield stacks and light-field volumes reconstructed with synthetic refocusing. Lateral and axial single-frame structural profiles from a single-cell filled with CaSiR-1 dye are shown. The lateral profiles are plotted at (a1) the native focal plane from widefield stacks, and light-field volumes reconstructed with (a2) synthetic refocusing and (a3) three-iteration RL deconvolution. The axial profiles have been extracted from the lateral position intersected by the red dashed lines at depths ranging from -40 to $+40$ μm. Increasing deconvolution iteration number increases both (b1) the lateral and (b2) axial signal confinement compared to synthetically refocused volumes. The deconvolved FWHMs are normalized to that of synthetic refocusing. The gray lines are from three different cells, and the red line is the average. Deconvolved light-fields (three-iteration RL, black solid line, and 21-iteration RL, red dashed line) features better (c1) lateral and (c2) axial spatial confinement than widefield z-stacks and synthetically refocused light-field volumes (Video 2, mp4, 8890 KB [URL: https://doi.org/10.1117/1.NPh.9.4.041404.2]).

Table 1 Summary of FWHM from single-cell labeled spatial profiles. Reported as median [IQR], $n = 3$.

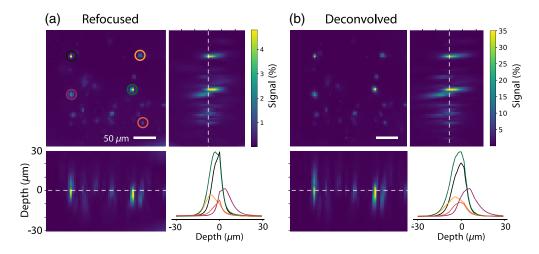|	Widefield	Refocused	Deconvolved[a]	
x	10.3 [7.1, 19.6]	13.5 [10.3, 15.0]	10.2 [7.3, 10.9]	μm
y	13.1 [9.0, 21.6]	9.1 [8.2, 12.9]	6.5 [6.2, 9.3]	μm
xz	17.9 [19.2, 34.4]	15.1 [10.6, 17.3]	10.4 [6.5, 12.4]	μm

[a]3-iteration RL.

Fig. 4 Reconstructed light-field volumes can distinguish active cells from different axial planes in bulk-labeled slices. Planes from bulk-labeled slices were reconstructed from light-field volumes with (a) synthetic refocusing and (b) 3D deconvolution (three-iteration RL) between -30 and $+30$ μm in steps of 1 μm. An activation map was generated from the variance of $\Delta F/F$ over time to identify active neurons. A maximum intensity projection through z was generated. A xz and yz maximum intensity projection shows multiple active cells in the field of view spanning different axial planes. The lower right plot in each panel shows the z-profiles of cellular ROIs circled in the same colors on the image. The center of mass of each neuron ranges in depth from -5 to $+4$ μm.

unachievable with any widefield imaging system. The center of mass of each neuron ranges from depths of -5 to $+4$ μm. The image contrast is higher for 3D deconvolved than for refocused volumes.

In addition, maximum intensity projections through xz and yz were generated with the TV term (Fig. S1D in the Supplemental Material). The TV term at both 10 and 30 iterations did not change the spatial signal confinement.

3.3 Light-Field Microscopy Resolves Calcium Signals from Neuronal Dendrites in 3D

LFM enables single-frame 3D imaging; therefore, we investigated its application to resolving calcium signals from neuronal processes in three spatial dimensions. We reconstructed 4D (x, y, z, t) light-field volumes from time series and extracted temporal signals from ROIs manually defined over dendrites from the $\Delta F/F$ activation map.

Depth-time plots were extracted from ROIs taken from light-field time series reconstructed with synthetic refocusing [Fig. 5(b)] and 3D deconvolution [three-iteration RL; Fig. 5(c)]. A depth map cannot be produced from widefield images as they are focused on a single axial plane [Fig. 5(a)]. Moreover, in contrast with Fig. 3, which displayed structural data, Fig. 5 shows functional activation maps in which the dendrites feature highest $\Delta F/F$ and therefore appear bright with respect to the soma. The signals as a function of depth were summed over time for each ROI to generate functional depth profiles [Figs. 5(d1)–5(d3)].

The peak dendritic $\Delta F/F$ signals are greater in deconvolved volumetric light-field time series [Figs. 5(c2)–5(c4)] compared with those synthetically refocused [Figs. 5(b2)–5(b4)], in agreement with the results from Sec. 3.1. From the depth plots, it appears that the center of mass of Area 3 lies near the native focal plane whereas Areas 1 and 2 lie deeper in the slice [Figs. 5(d1)–5(d3)]. This indicates that calcium transients can be resolved from neuronal subcompartments in axially distinct planes.

The decay time, measured by the FWHM of somatic calcium transients at the native focal plane, is the same between widefield (0.23 [0.20, 0.27]s, $n = 3$ cells) and light-field time series reconstructed with synthetic refocusing (soma: 0.24 [0.21, 0.32]s, $n = 3$ cells) and 3D deconvolution (soma: 0.22 [0.20, 0.40]s, $n = 3$ cells). Moreover, there is no significant difference
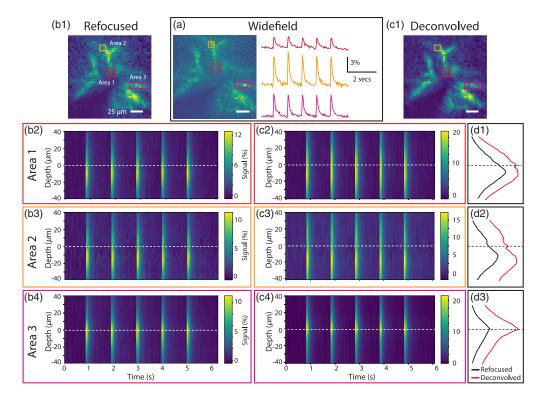
Fig. 5 Calcium signals in dendrites can be observed across axially distinct planes from single-cell light-field volumes. (a) The activation (or variance) map from a widefield image series with time courses extracted from three dendritic ROIs (red, orange, and pink outlines). Depth-time plots are shown from the same ROIs reconstructed from a light-field time series with (b) synthetic refocusing and (c) 3D deconvolution. (d1)–(d3) The sum of the signal over time as a function of depth in the three dendritic ROIs.

between the decay time of dendritic signals of synthetically refocused (dendrite: 0.139 [0.136, 0.141]s, $n = 3$ cells) or deconvolved (dendrite: 0.132 [0.126, 0.167]s, $n = 3$ cells) light-field time series.

4 Discussion

We resolved CaSiR-1 fluorescence transients in single cells and bulk-labeled live mouse brain slices. We found that calcium transient tSNR from bulk-labeled slices did not differ between widefield and light-field time series reconstructed with synthetic refocusing and three-iteration RL 3D deconvolution. For single-labeled cells, the tSNR was significantly larger for light-field time series reconstructed with three-iteration RL 3D deconvolution compared to synthetic refocusing. In bulk-labeled slices, deconvolution increases both the peak signal and the noise, resulting in tSNR similar to that obtained by synthetic refocusing after three iterations. Noise amplification with deconvolution has a greater effect on tSNR in the bulk-labeled cells compared to single-labeled cells perhaps due to the high level of background fluorescence. Increasing the number of deconvolution iterations increased signal size and noise but reduced tSNR. Increased iteration number also increased signal confinement. Both light-field reconstruction algorithms, synthetic refocusing and RL deconvolution, enabled 3D localization of calcium transients in single dye-loaded neurons and bulk-labeled slices. Extracting calcium transients from light fields, compared with widefield image time series, did not incur any penalty in terms of tSNR, while enabling volumetric imaging.

The reduction in tSNR seen from deconvolved volumes arises from noise amplification due to lack of regularization.[30] To reduce noise amplification, fewer iteration numbers provide a regularizing effect on the deconvolution.[13] For higher iteration numbers, we attempted to overcome noise amplification by implementing TV-regularization in the RL deconvolution.[30]

However, this yielded no benefit in terms of signal, noise, or tSNR in the extracted calcium time series.

RL deconvolution at high iteration numbers decreases tSNR, and moreover increases computational cost compared with synthetic refocusing. In our implementation and hardware, reconstructing a volume (20 μm) with synthetic refocusing took 40 s per frame while RL deconvolution took 20 s per iteration per frame (Processor i7 CPU @ 3.6 GHz, RAM 32 GB). A typical time series consisted of 200 frames (2048 × 2048 pixels, 20 Hz for 10 s). Reconstructing volumes (20 μm) for the full time series took ∼2 h with synthetic refocusing, 3.5 h three-iteration RL deconvolution, and 22 h with 20-iteration RL deconvolution. Methods to increase speed without the need to use high performance computing are desirable. Reconstruction speed has been improved by a number of groups through deep learning solutions.[19,33] We have shown that 3D deconvolution achieves higher spatial signal confinement than synthetic refocusing with axial confinement increasing at high iteration numbers. Therefore, to maximize spatial signal confinement a time-consuming iterative deconvolution technique could be beneficial.

Deconvolution algorithms leverage the fine sampling of individual projections through the volume, whereas refocusing cannot. Here, we used a coarse deconvolution approach. Lateral oversampling can further improve the lateral signal confinement, providing lateral sampling rates greater than the native LFM resolution. However, oversampling increases computational cost and was unnecessary here as the LFM was designed for cellular resolution. We used the original light-field microscope design.[7] Fourier LFM, where the MLA is placed at the aperture stop of the microscope objective instead of the image plane, has also been shown to improve the lateral sampling rate even in the degenerate native focal plane.[34–37]

Both synthetic refocusing and 3D deconvolution reconstruction algorithms rely on ballistic photons, limiting their application in highly scattering mammalian brains. To minimize scattering, we used a red-emitting calcium dye, CaSiR-1, the emission of which is less scattered than shorter wavelength emitting fluorophores. Furthermore, deep near-infrared indicators can be combined with blue-light-sensitive opsins to achieve spectrally cross-talk free all-optical neurophysiology[38,39] or combined with shorter wavelength emitting fluorophores for imaging in multiple spectral channels.[40] In our experiments, calcium signal extraction from reconstructed volumes was limited to depths of ∼50 μm, within the photon mean-free path. In addition to scattering effects, our calcium dye loading was constrained to the superficial cell layers. *In-vivo* in mouse cortex, GCaMP6m time-series extraction from light fields was previously demonstrated at depths up to 380 μm.[20] Methods to improve signal extraction in scattering tissue have been demonstrated by computationally extracting fluorescence sources without reconstruction,[15,20,22,41–43] although reconstruction-less signal extraction cannot resolve the propagation of calcium signals throughout spatially extended structures such as dendrites. Combining the principles of confocal microscopy with LFM,[44] selective-volume illumination,[19,45,46] and/or spatially sparse labeling with genetically encoded indicators can increase contrast to enable calcium signal extraction from reconstructed volumes at greater depths.

We detected dendritic calcium signals, evoked by backpropagating action potentials, in intracellularly dye loaded single cells. Limited dye diffusion precluded activity detection in distant processes. Applying LFM to neuronal tissues expressing genetically encoded calcium indicators sparsely and strongly may enable tracing of functional signals through dendrites in three-dimensions, or synaptic mapping. Similar analyses have been performed for sparsely labeled genetically encoded voltage indicators (GEVIs) with a much lower baseline fluorescence, $\Delta F/F$, and tSNR than that of the CaSIR-1 calcium dye.[47,48] Quicke et al. also demonstrated axial resolution of GEVI signals from dendrites at different depths. In combination with the present study, these results describe the LFM's capacity to resolve function neuronal signals volumetrically at subcellular resolution in both low and high tSNR regimes. LFM captures 3D information with significantly reduced imaging time and bleaching compared to widefield. Generating similar 3D volumes in widefield would require physical refocusing of the objective in between trials. Our comparison of widefield trials to light-field trials reconstructed at the same axial plane revealed no penalty in terms of extracted calcium transient tSNR for light fields, which additionally enabled extraction of "in-focus" calcium transients from axially separated planes. Optically, implementing LFM is simple and low-cost, requiring only the introduction

an off-the-shelf MLA at the native imaging plane of a standard widefield epifluorescence microscope. Cost-effective sCMOS cameras feature sensitivities and bandwidths well adapted to calcium LFM. Calcium imaging applications requiring high volume acquisition rates can readily benefit from LFM's ability to trade spatial resolution for the ability to excite and image fluorescence simultaneously throughout a volume.

These results demonstrate the capabilities and limitations of two light-field reconstruction algorithms for high tSNR calcium fluorescence imaging. The trade-offs described above highlight the importance of adapting the volume reconstruction strategy to the scientific goals and requirements of future neurophysiology experiments. For example, applications requiring online analysis to guide the experimental protocols would benefit from the speed and simplicity of synthetic refocusing or low iteration-number 3D RL deconvolution. We found that calcium signal extraction from volumes reconstructed with three-iteration 3D RL deconvolution yielded high tSNR while bringing lateral signal confinement near to the maximum. However, higher iteration numbers, while decreasing tSNR, continued improving the axial confinement. These results demonstrate the importance characterizing and balancing tSNR, spatial signal confinement, and computational cost when selecting a volume reconstruction method for functional LFM applications.

Disclosures

The authors declare no conflicts of interest.

Acknowledgments

Data, Materials, and Code Availability

The datasets and code generated for this study are available on request to the corresponding author.

References

1. F. Ali and A. C. Kwan, "Interpreting *in vivo* calcium signals from neuronal cell bodies, axons, and dendrites: a review," *Neurophotonics* **7**(1), 011402 (2019).
2. H. Dana et al., "Sensitive red protein calcium indicators for imaging neural activity," *Elife* **5**, e12727 (2016).
3. M. Z. Lin and M. J. Schnitzer, "Genetically encoded indicators of neuronal activity," *Nat. Neurosci.* **19**(9), 1142 (2016).
4. J. Platisa and V. A. Pieribone, "Genetically encoded fluorescent voltage indicators: are we there yet?" *Curr. Opin. Neurobiol.* **50**, 146–153 (2018).
5. V. Grenier et al., "Spying on neuronal membrane potential with genetically targetable voltage indicators," *J. Am. Chem. Soc.* **141**(3), 1349–1358 (2019).
6. M. A. Popovic et al., "Electrical behaviour of dendritic spines as revealed by voltage imaging," *Nat. Commun.* **6**, 8436 (2015).
7. M. Levoy et al., "Light field microscopy," in *ACM SIGGRAPH 2006 Papers on - SIGGRAPH '06*, p. 924 (2006).
8. M. Broxton et al., "Wave optics theory and 3-D deconvolution for the light field microscope," *Opt. Express* **21**(21), 25418 (2013).

9. P. Quicke et al., "Calculation of high numerical aperture lightfield microscope point spread functions," in *Comput. Opt. Sens. and Imaging*, Optical Society of America, p. CW4A-2 (2019).

10. W. H. Richardson, "Bayesian-based iterative method of image restoration," *J. Opt. Soc. Am.* **62**, 55 (1972).

11. L. B. Lucy, "An iterative technique for the rectification of observed distributions," *Astron. J.* **79**, 745 (1974).

12. M. E. Daube-Witherspoon and G. Muehllehner, "An iterative image space reconstruction algorithm suitable for volume ECT," *IEEE Trans. Med. Imaging* **5**, 61–66 (1986).

13. M. Bertero, P. Boccacci, and V. Ruggiero, *Inverse Imaging with Poisson Data*, IOP Publishing, Bristol (2018).

14. R. Prevedel et al., "Simultaneous whole-animal 3D imaging of neuronal activity using light-field microscopy," *Nat. Methods* **11**(7), 727–730 (2014).

15. N. C. Pégard et al., "Compressive light-field microscopy for 3D neural activity recording," *Optica* **3**(5), 517 (2016).

16. L. Cong et al., "Rapid whole brain imaging of neural activity in freely behaving larval zebra-fish (*Danio rerio*)," *eLife* **6**, e28158 (2017).

17. M. A. Taylor et al., "Brain-wide 3D light-field imaging of neuronal activity with speckle-enhanced resolution," *Optica* **5**(4), 345–353 (2018).

18. S. Aimon et al., "Fast near-whole–brain imaging in adult drosophila during responses to stimuli and behavior," *PLoS Biol.* **17**(2), e2006732 (2019).

19. Z. Wang et al., "Real-time volumetric reconstruction of biological dynamics with light-field microscopy and deep learning," *Nat. Methods* **18**(5), 551–556 (2021).

20. T. Nöbauer et al., "Video rate volumetric Ca^{2+} imaging across cortex using seeded iterative demixing (SID) microscopy," *Nat. Methods* **14**(8), 811–818 (2017).

21. L. Grosenick et al., "Identification of cellular-activity dynamics across large tissue volumes in the mammalian brain," bioRxiv, 132688 (2017).

22. O. Skocek et al., "High-speed volumetric imaging of neuronal activity in freely moving rodents," *Nat. Methods* **15**(6), 429–432 (2018).

23. T. Egawa et al., "Development of a far-red to near-infrared fluorescence probe for calcium ion and its application to multicolor neuronal imaging," *J. Am. Chem. Soc.* **133**(36), 14157–14159 (2011).

24. C. L. Howe et al., "Comparing wide field to 3D light field for imaging red calcium transients in mammalian brain," in *Opt. and the Brain*, Optical Society of America, p. BTu2C-4 (2020).

25. Z. Zhang, *A Practical Introduction to Light Field Microscopy*, pp. 1–15, Computer Graphics Laboratory. Electrical Engineering, Stanford University (2010).

26. J. T. Ting et al., "A robust *ex vivo* experimental platform for molecular-genetic dissection of adult human neocortical cell types and circuits," *Sci. Rep.* **8**(1), 8407 (2018).

27. R. Franconville et al., "Somatic calcium level reports integrated spiking activity of cerebellar interneurons *in vitro* and *in vivo*," *J. Neurophysiol.* **106**(4), 1793–1805 (2011).

28. A. D. Edelstein et al., "Advanced methods of microscope control using μ manager software," *J. Biol. Methods* **1**(2), e10 (2014).

29. R. Ng et al., "Light field photography with a hand-held plenoptic camera – Stanford Tech Report CTSR 2005-02," Technical Report (2005).

30. N. Dey et al., "Richardson-Lucy algorithm with total variation regularization for 3D confocal microscope deconvolution," *Microsc. Res. Tech.* **69**(4), 260–266 (2006).

31. P. Virtanen et al., "SciPy 1.0: fundamental algorithms for scientific computing in Python," *Nat. Methods* **17**, 261–272 (2020).

32. R. L. White, "Image restoration using the damped Richardson-Lucy method," *Proc. SPIE* **2198**, 1342–1348 (1994).

33. J. P. Vizcaíno et al., "Learning to reconstruct confocal microscopy stacks from single light field images," *IEEE Trans. Comp. Imaging* **7**, 775–788 (2021).

34. A. Llavador et al., "Resolution improvements in integral microscopy with Fourier plane recording," *Opt. Express* **24**(18), 20792–20798 (2016).

35. C. Guo et al., "Fourier light-field microscopy," *Opt. Express* **27**, 25573–25594 (2019).
36. A. Stefanoiu et al., "What about computational super-resolution in fluorescence Fourier light field microscopy?" *Opt. Express* **28**(11), 16554–16568 (2020).
37. F. L. Liu et al., "Fourier diffuserscope: single-shot 3D Fourier light field microscopy with a diffuser," *Opt. Express* **28**(20), 28969–28986 (2020).
38. J. Akerboom et al., "Genetically encoded calcium indicators for multi-color neural activity imaging and combination with optogenetics," *Front. Mol. Neurosci.* **6**, 2 (2013).
39. N. S. Soor et al., "All-optical crosstalk-free manipulation and readout of chronos-expressing neurons," *J. Phys. D: Appl. Phys.* **52**(10), 104002 (2019).
40. M. Oheim et al., "New red-fluorescent calcium indicators for optogenetics, photoactivation and multi-color imaging," *Biochim. Biophys. Acta-Mol. Cell Res.* **1843**(10), 2284–2306 (2014).
41. P. Song et al., "3D localization for light-field microscopy via convolutional sparse coding on epipolar images," *IEEE Trans. Comput. Imaging* **6**, 1017–1032 (2020).
42. P. Song et al., "Model-inspired deep learning for light-field microscopy with application to neuron localization," in *ICASSP 2021-2021 IEEE Int. Conf. Acoust., Speech and Signal Process. (ICASSP)*, IEEE, pp. 8087–8091 (2021).
43. H. Verinaz-Jadan et al., "Deep learning for light field microscopy using physics-based models," in *IEEE 18th Int. Symp. Biomed. Imaging (ISBI)*, IEEE, pp. 1091–1094 (2021).
44. Z. Zhang et al., "Imaging volumetric dynamics at high speed in mouse and zebrafish brain with confocal light field microscopy," *Nat. Biotechnol.* **39**, 74–83 (2020).
45. T. V. Truong et al., "High-contrast, synchronous volumetric imaging with selective volume illumination microscopy," *Commun. Biol.* **3**(1), 74 (2020).
46. S. Madaan et al., "Single-objective selective-volume illumination microscopy enables high-contrast light-field imaging," *Opt. Lett.* **46**(12), 2860–2863 (2021).
47. P. Quicke et al., "Subcellular resolution three-dimensional light-field imaging with genetically encoded voltage indicators," *Neurophotonics* **7**(3), 035006 (2020).
48. P. Quicke et al., "Single-neuron level one-photon voltage imaging with sparsely targeted genetically encoded voltage indicators," *Front. Cell. Neurosci.* **13**, 39 (2019).

Carmel L. Howe is a research associate at Imperial College London, United Kingdom. She received her MEng and PhD degrees in electrical and electronic engineering from the University of Nottingham in 2014 and 2018, respectively. She is currently developing a new high-speed, high-throughput, three-dimensional imaging modality based on light-field microscopy to track network-level neuronal activity in the mammalian brain. Her research combines the fields of neurophysiology, optical engineering, signal and image processing.

Peter Quicke is a postdoctoral research associate in the Department of Bioengineering at Imperial College London. He received his MSci (with BSc) degree in physics in 2014, his MRes. Degree in neurotechnology in 2015, and his PhD in 2019. His current research interests include computational microscopy and functional voltage imaging.

Pingfan Song is a research associate at Imperial College London. He received his PhD from the University College London, his master's and bachelor's degrees both from Harbin Institute of Technology. His research interests lie in signal/image processing, machine learning, and computational imaging with applications on a variety of image modalities.

Herman Verinaz-Jadan received his bachelor's degree in electronic and communications engineering from Escuela Superior Politecnica del Litoral, Ecuador, his master's degree from Imperial College London, United Kingdom. He is currently working toward his PhD in the Department of Electrical and Electronic Engineering, Imperial College London, United .ingdom. His research interests include sparsity-driven signal processing, machine learning with applications in inverse problems. He is currently funded by the EEE Department of Imperial College London.

Pier Luigi Dragotti received his Laurea degree (summa cum laude) in electronic engineering from the University Federico II, Naples, Italy, in 1997, his master's degree in communications

systems from the Swiss Federal Institute of Technology of Lausanne (EPFL), Switzerland, in 1998, and his PhD from EPFL, Switzerland, in April 2002. He has held several visiting positions. In particular, he was a visiting student at Stanford University, Stanford, California, USA, in 1996, a summer researcher at the Mathematics of Communications Department, Bell Labs, Lucent Technologies, Murray Hill, New Jersey, USA, in 2000, and a visiting scientist at the Massachusetts Institute of Technology in 2011. He is currently a professor of signal processing with the Electrical and Electronic Engineering Department, Imperial College London. Before joining Imperial College in November 2002, he was a senior researcher at EPFL, working on distributed signal processing for sensor networks for the Swiss National Competence Center in Research on Mobile Information and Communication Systems. His research interests include sampling theory, wavelet theory and its applications, sparsity-driven signal processing with application in image super-resolution, neuroscience, and computational imaging. He was the technical cochair of the European Signal Processing Conference in 2012, an associate editor of the IEEE Transactions on Image Processing from 2006 to 2009, a member of the IEEE Image, Video and Multidimensional Signal Processing Technical Committee, and a member of the IEEE Signal Processing Theory and Methods Technical Committee. He was also a recipient of the ERC Investigator Award. He is currently the editor-in-chief of the IEEE Transactions on Signal Processing, and a member of the IEEE Computational Imaging Technical Committee and a fellow of the IEEE.

Amanda J. Foust is a royal academy of engineering research fellow and lecturer in the Department of Bioengineering at Imperial College London. She studied neuroscience with emphasis in computation and electrical engineering (BSc degree) at Washington State University, and Neuroscience (MPhil, PhD) at Yale University. The aim of her research program is to engineer bridges between cutting-edge optical technologies and neuroscientists to acquire new, ground-breaking data on how brain circuits wire, process, and store information.